Report

Cell Reports

Chiral Cilia Orientation in the Left-Right Organizer

Graphical Abstract

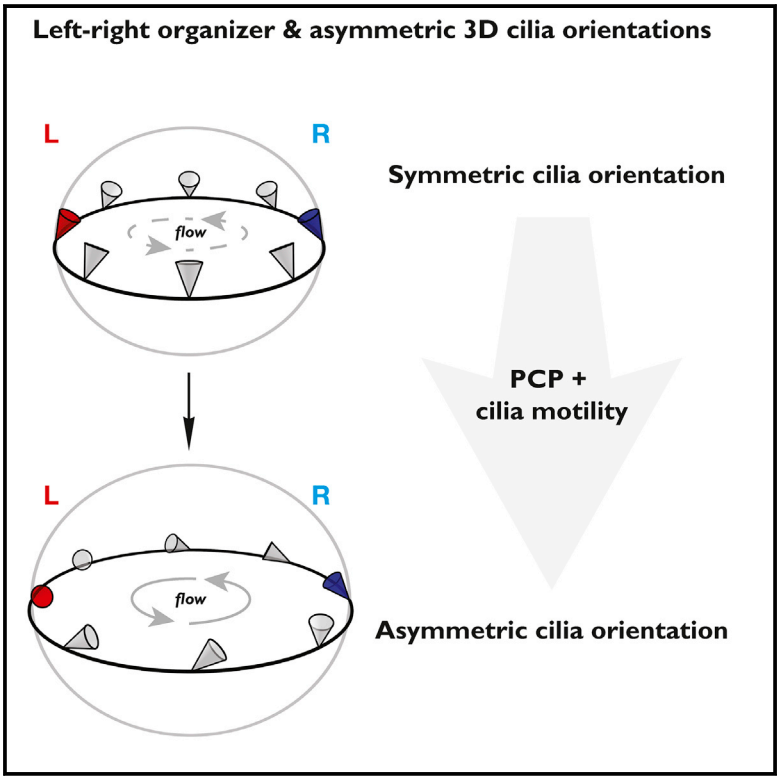

Highlights

- KV cilia display asymmetric orientation between the right and left sides
- Cilia orientation depends on PCP, but does not directly follow its direction
- Impact of asymmetric cilia orientation on left-right symmetry breaking is unclear
- Asymmetric cilia orientation is independent of left-right signaling pathway or flow

Authors

Rita R. Ferreira, Guillaume Pakula, Lhéanna Klaeyle, Hajime Fukui, Andrej Vilfan, Willy Supatto, Julien Vermot

Correspondence

julien@igbmc.fr

In Brief

During left-right axis specification, motile cilia are required for breaking the axis of symmetry. In this context, Ferreira et al. show that cilia orientation is chiral, defining an alternative type of asymmetry in the embryo.

Ferreira et al., 2018, Cell Reports *25*, 2008–2016
November 20, 2018
https://doi.org/10.1016/j.celrep.2018.10.069

CellPress

OPEN ACCESS
CellPress

Cell Reports
Report

Chiral Cilia Orientation in the Left-Right Organizer

Rita R. Ferreira,[1,2,3,4] Guillaume Pakula,[5] Lhéanna Klaeyle,[1,2,3,4] Hajime Fukui,[1,2,3,4] Andrej Vilfan,[6,7] Willy Supatto,[5] and Julien Vermot[1,2,3,4,8,*]

[1]Institut de Génétique et de Biologie Moléculaire et Cellulaire, Illkirch, France
[2]Centre National de la Recherche Scientifique, UMR7104, Illkirch, France
[3]Institut National de la Santé et de la Recherche Médicale, U1258, 67404 Illkirch, France
[4]Université de Strasbourg, Illkirch, France
[5]Laboratory for Optics and Biosciences, Ecole Polytechnique, Centre National de la Recherche Scientifique (UMR7645), Institut National de la Santé et de la Recherche Médicale (U1182), Palaiseau, France
[6]J. Stefan Institute, Ljubljana, Slovenia
[7]Max Planck Institute for Dynamics and Self-Organization (MPIDS), 37077 Göttingen, Germany
[8]Lead Contact
*Correspondence: julien@igbmc.fr
https://doi.org/10.1016/j.celrep.2018.10.069

SUMMARY

Chirality is a property of asymmetry between an object and its mirror image. Most biomolecules and many cell types are chiral. In the left-right organizer (LRO), cilia-driven flows transfer such chirality to the body scale. However, the existence of cellular chirality within tissues remains unknown. Here, we investigate this question in Kupffer's vesicle (KV), the zebrafish LRO. Quantitative live imaging reveals that cilia populating the KV display asymmetric orientation between the right and left sides, resulting in a chiral structure, which is different from the chiral cilia rotation. This KV chirality establishment is dynamic and depends on planar cell polarity. While its impact on left-right (LR) symmetry breaking remains unclear, we show that this asymmetry does not depend on the LR signaling pathway or flow. This work identifies a different type of tissue asymmetry and sheds light on chirality genesis in developing tissues.

INTRODUCTION

A chiral object cannot be superimposed on its mirror image. Most biological molecules are chiral. However, how macroscopic chiral asymmetries arise in physics and biology is still debated (Morrow et al., 2017; Wagnière, 2007). In living systems, a number of independent mechanisms of chirality establishment have been identified, from the subcellular to the tissue scale (Blum et al., 2014a; Coutelis et al., 2014; Dasgupta and Amack, 2016; Gómez-López et al., 2014; Hamada and Tam, 2014; Levin, 2005; Naganathan et al., 2014; Noël et al., 2013; Tee et al., 2015). The most studied system is certainly the mechanism that sets asymmetric gene expression around the left-right organizers (LROs) of vertebrates (Ferreira and Vermot, 2016; Blum et al., 2014b; Vandenberg and Levin, 2013; Freund et al., 2012). In general, asymmetrical signals are generated in LROs as a response to a directional flow driven by motile cilia (Shinohara and Hamada, 2017). In the LRO, clockwise cilia rotation is invariable among vertebrates (Okada et al., 2005). These properties are key for controlling the chiral flow (Hilfinger and Jülicher, 2008; Shinohara and Hamada, 2017; Supatto and Vermot, 2011). Nevertheless, other cellular chiral features at the scale of the whole LRO have never been investigated.

In zebrafish, the LRO is called Kupffer's vesicle (KV) (Figure 1A). Before any sign of asymmetric cell response, the KV consists of a sphere containing monociliated cells in which a directional flow emerges as a result of stereotyped cilia spatial orientation (Ferreira et al., 2017). Over a few hours, the cilia-generated flow triggers an asymmetric calcium response on the left side of the cavity (Francescatto et al., 2010; Sarmah et al., 2005; Yuan et al., 2015) and, consequently, a left-biased asymmetric pattern of gene expression (Essner et al., 2005; Kramer-Zucker et al., 2005). Coordinating appropriate cilia spatial orientation with directional flow generation is therefore critical for the asymmetric response and proper left-right (LR) patterning (Hashimoto and Hamada, 2010). Current studies propose that flow patterns arise first in the LRO and then dictate the symmetry-breaking event (Blum et al., 2014a; Shinohara and Hamada, 2017). This suggests that symmetry breaking initiation depends on the establishment of symmetrical LRO, in which cilia orientation is tightly controlled by the planar cell polarity (PCP) pathway (Hashimoto and Hamada, 2010; Marshall and Kintner, 2008; Song et al., 2010). In this model, the sense of cilia rotation leading to the directional flow is the only known chiral element in the LRO. However, several studies have suggested that subcellular chirality associated with cytoskeletal asymmetric order could also participate in setting the LR axis—in particular, in asymmetric animals in which no LROs have been identified (Davison et al., 2016; Hozumi et al., 2006; Kuroda et al., 2009; Sato et al., 2015; Shibazaki et al., 2004; Spéder et al., 2006; Inaki et al., 2018; Wan et al., 2016). This raises the intriguing possibility that the LRO could use subcellular chiral information for symmetry breaking. In the absence of tools for visualizing potential chirality in the LRO, however, it is difficult to establish whether cell chirality could participate in the process of symmetry breaking.

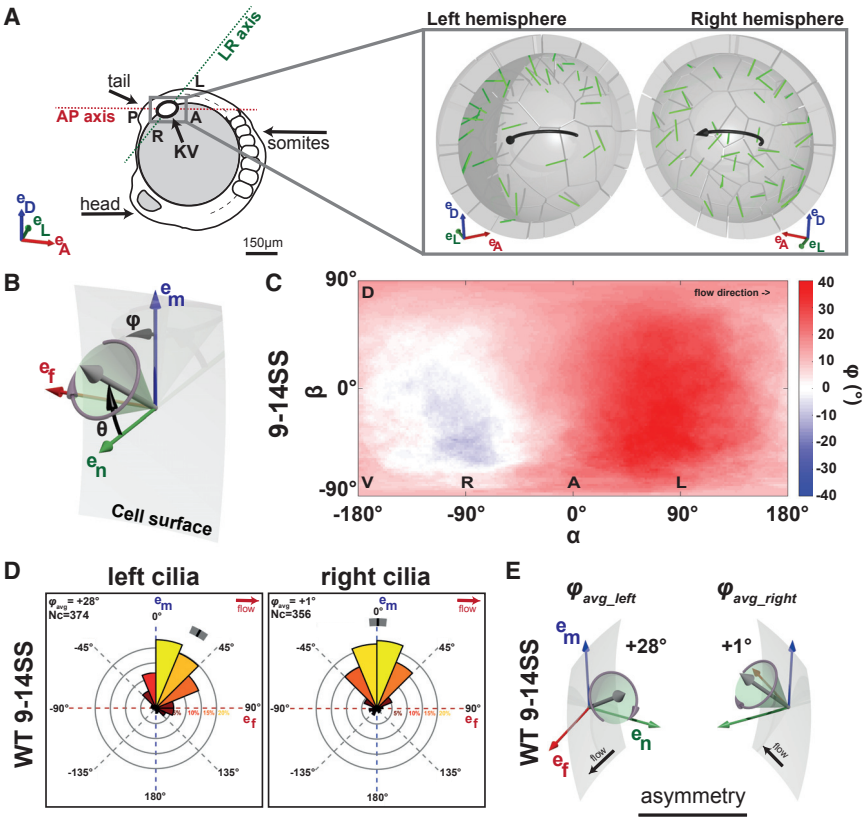

Figure 1. The Zebrafish Left-Right Organizer Is Asymmetric

(A) The zebrafish embryo (left) highlighting the KV (gray box). The zoom-up box (right) shows the transverse section of the KV, depicting the cilia (green) and the directional flow (black arrows). The embryonic body plan axes are marked as AP (anterior-posterior) and LR (left-right). The body plan reference frame is defined by basis vectors e_D (dorsal), e_L (left), and e_A (anterior).

(B) Cilia orientations are represented by two angles: θ (tilt angle from the surface normal e_n) and φ (angle between the surface projection of the ciliary vector and the meridional direction e_m). Cell surface is represented in gray, e_m in blue, e_f in red, and the normal e_n in green.

(C and D) Distributions of φ at 9–14SS obtained from 14 wild-type vesicles with 730 cilia. (C) Average φ values displayed in a 2D flat map showing that ϕ is higher on the left ($0° \leq \alpha \leq 180°$, red) than on the right ($-180° \leq \alpha \leq 0°$, blue). ($\alpha$,$\beta$) are spherical coordinates on the KV surface with (0,0) at the anterior pole (Ferreira et al., 2017).

(D) φ angle distribution of left- and right-sided motile cilia (black tick, population mean; gray stripe, 95% confidence interval [CI]): 0° indicates the meridional (e_m) and 90° the flow direction (e_f). N_c, number of cilia.

(E) Orientation of the 3D resultant vector on the left and right sides of the KV.

See also Figure S1.

To meet this challenge, we developed a quantitative analysis based on live imaging, allowing the investigation of the LRO chirality and the identification of the factors controlling it.

RESULTS

Tissue chirality can result from asymmetric cell shape and asymmetric organelle distribution at the cell scale (Wan et al., 2011; Xu et al., 2007). We reasoned that as an asymmetry generator, the LRO itself constitutes a candidate for being a chiral organ. We used the KV ellipsoidicity to assess the symmetry of cilia orientation by focusing on the two angles defining cilia orientation in three dimensions (3D) (Figure 1B): θ (tilt) is the angle of the cilium with respect to the KV surface normal (0° for a cilium orthogonal to the KV surface and 90° for parallel); φ is the orientation of the cilium projected on the KV surface (0° for a cilium pointing in a meridional direction). Thus, the meridional tilt of cilia reported in wild-type (WT) corresponds to $\theta > 0°$ and φ close to 0°, meaning that cilia point dorsally following the meridians of a sphere (Ferreira et al., 2017; Supatto et al., 2008). We performed live imaging using the zebrafish *act2b:Mmu.Arl13bGFP* transgenic line in which cilia are fluorescently labeled (Borovina et al., 2010). We extracted the angles θ_{avg} and φ_{avg} of the average cilia orientation vector in both hemispheres of the KV between 9SS (somite stage) and 14SS, when the chiral flow is fully established. To quantify differences in cilia orientation between the left and right sides, we calculated the average cilium direction in local coordinates for each side (Figure 1B). Analogous to individual cilia, the angles φ_{avg} and θ_{avg} describe the direction of the average orientation vector on each side. In case of a mirror-symmetric KV, θ_{avg} of the average cilium is equal on the left and right sides and the ϕavg angles are mirror imaged: $\theta_{avg\_left} = \theta_{avg\_right}$, and $\varphi_{avg\_left} = -\varphi_{avg\_right} = \varphi_{avg\_right\_mirror}$. To quantitatively assess the significance of asymmetries in the KV, we used a permutation test based on the definition of chirality (see STAR Methods) and calculated p values estimating the likelihood that an *a priori* symmetric KV will show an equal or larger difference $|\varphi_{avg\_left} - \varphi_{avg\_right\_mirror}|$ due to variability.

We extracted and averaged the results obtained from 14 WT vesicles with a total of 730 cilia and estimated the θ_{avg} and φ_{avg} angles of the average cilium in 3D. There was a difference between the measured φ angle on the left and the right sides of the KV (Figure 1C). While right-sided cilia are almost perfectly oriented along the meridional direction ($\varphi_{avg\_right} = +1°$; Figures 1D and 1E), cilia in the left hemisphere exhibit a strong tilt following the flow direction ($\varphi_{avg\_left} = +28°$; Figures 1D and 1E). On average, it defines a dextral orientation (Figure S2A). The permutation test confirmed the significance ($p < 0.001$) of the asymmetric cilia orientations between the left and right sides ($\varphi_{avg\_left} \neq -\varphi_{avg\_right}$) (STAR Methods; Table S1). No difference in tilt angles was observed between the left and right sides ($\theta_{avg\_left} = \theta_{avg\_right}$; Figure S1A). These results show that cilia orientation is asymmetric in the KV and follows a dextral chirality.

To gain a better sense of when the chirality of cilia orientation begins, we analyzed cilia orientation in embryos at different

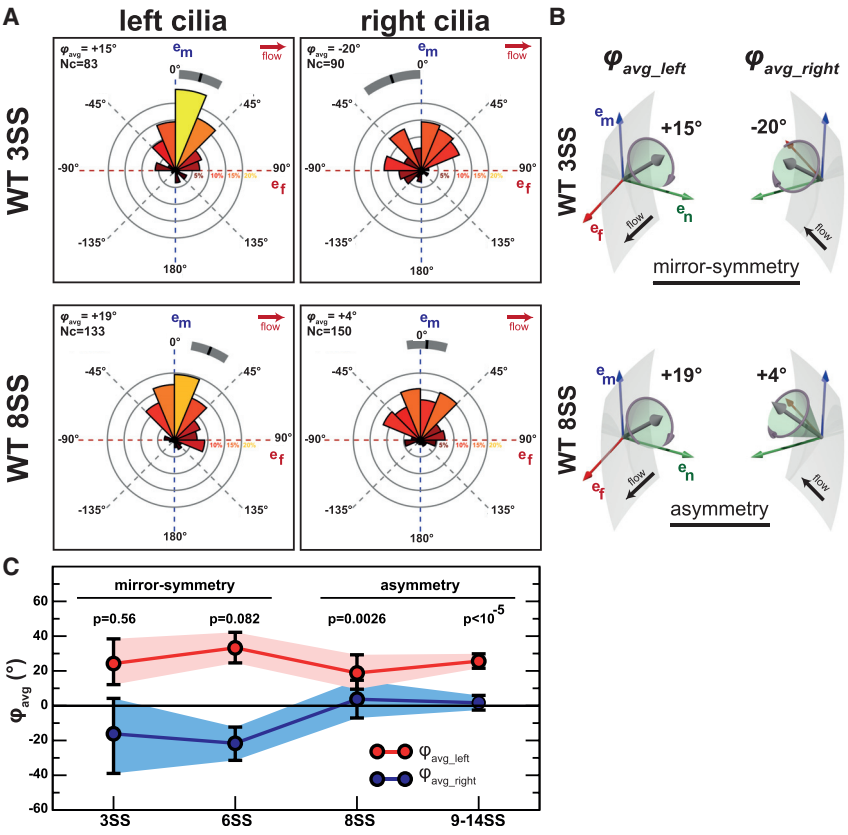

Figure 2. Asymmetric Cilia Orientation Arises over Time

(A) φ angle distributions of the left-sided (left) and right-sided (right) cilia for WT 3SS (upper) and WT 8SS (lower).

(B) φ_{avg} on the left and right sides at 3SS and 8SS.

(C) Mean orientation φ_{avg} of motile cilia in the left (red) and right (blue) half of the KV as a function of time (error bars, 95% CI).

See also Figures S1, S2, and S3.

developmental stages. We quantified φ angle distributions of cilia from both hemispheres of WT embryos at 3SS (early stage), when the first signs of LR asymmetry have been reported (Yuan et al., 2015), at 6SS, and at 8SS (mid-stages). At 3SS, two populations of cilia exist, motile and immotile. Neither the motile (φ_{avg_left} = +15° and φ_{avg_right} = −20°; Figures 2A and 2B) nor the immotile cilia population (φ_{avg_left} = +32° and φ_{avg_right} = −8°; Figure S2B) exhibit a significant difference between the left and right sides ($\varphi_{avg\_left} \approx -\varphi_{avg\_right}$; Table S1), resulting in a φ_{avg} close to 0° at 3SS (Figure 3A). WT embryos at 6SS show some asymmetry (Figure 3A) but are not yet significant (p = 0.086; Table S1). At 8SS the side-biased orientation (φ_{avg_left} = +19° and φ_{avg_right} = +4°; Figures 2A–2C) becomes significant, revealing an overall asymmetry (Figure 3A; Table S1). The orientation differences do not change linearly between left and right. The left angle does not change much between 3SS and 8SS, and the right side changes more significantly. The variability of cilia orientation (Figure S3A) is always substantial, but it reduces with time, and all 14 embryos at 9–14SS show asymmetry in the same direction. We did not detect any asymmetry in the distributions of θ angles, demonstrating that the cilia tilt remains symmetrical over time (Figure S1A). These results demonstrate that cilia orientation does not exhibit any asymmetry until 6SS and becomes progressively asymmetric during the course of KV development.

Considering that the KV generates an asymmetrical signal, we investigated whether the observed cilia asymmetry depends upon the LR signaling pathway. Pkd2 acts as a flow sensor and leads to left-sided expression of spaw, a nodal-related gene involved in establishing LR asymmetry (Schottenfeld et al., 2007; Yuan et al., 2015). To test the impact of flow sensing and asymmetric gene expression downstream of flow, we used *cup* (Schottenfeld et al., 2007) and *spaw* (Kalogirou et al., 2014) mutants in which *pkd2* and *spaw* are not functional with laterality defects (Figures S4B and S4C; Table S2). We found normal meridional orientation (Figure S2C, $\varphi_{avg} \neq 0°$ in Figure 3A) and asymmetry of cilia ($\varphi_{avg\_left} \neq -\varphi_{avg\_right}$) in *cup*$^{-/-}$ and *spaw*$^{-/-}$ KV cilia at 8SS. These results indicate that asymmetric cilia orientation is not dependent upon the LR signaling cascade.

Actomyosin contractility modulates tissue chirality *in vitro* (Wan et al., 2011) and *in vivo* (Qiu et al., 2005; Noël et al., 2013; Taber, 2006). In addition, it is important for the migration of the basal body to the apical surface of cells and is essential for cilia formation (Hong et al., 2015; Pitaval et al., 2010), KV morphogenesis (Wang et al., 2012), and LR determination (Gros et al., 2009; Tabin and Vogan, 2003; Wang et al., 2012). We therefore assessed its impact on asymmetric cilia orientation. We used blebbistatin and the *rock2b* morpholino (MO) to block Myosin-II activation (Wang et al., 2011). Blebbistatin-treated and *rock2b* MO embryos exhibit laterality defects (Figures S4B and S4C; Table S2) and abnormal cell clustering in the anterior side of the KV (Figure S1D), as previously described (Wang et al., 2011, 2012). Cilia orientation analysis showed that the Rock2b-Myosin II pathway does not interfere with the meridional tilt (Figure S2C) and asymmetric orientation at 8SS (Figure 3A; Table S1). These results indicate that asymmetric cilia orientation is not under the control of the main components of the LR signaling acting upstream and downstream of flow.

Ciliary components involved in motility can modulate cilia orientation (Jaffe et al., 2016). We therefore assessed whether cilia motility could cause asymmetric cilia orientation. We analyzed cilia orientation in WT at 3SS and found that immotile cilia have a distinct orientation compared to the motile cilia at the same stage ($\theta_{avg\_WT3SS\ immotile}$ = +15° and $\theta_{avg\_WT3SS\ motile}$ = +30°; $p < 10^{-4}$), suggesting that motility is modulating cilia orientation. To confirm cilia motility involvement, we analyzed the effects of *dnah9* (*lrdr1*) knockdown and found that asymmetric cilia

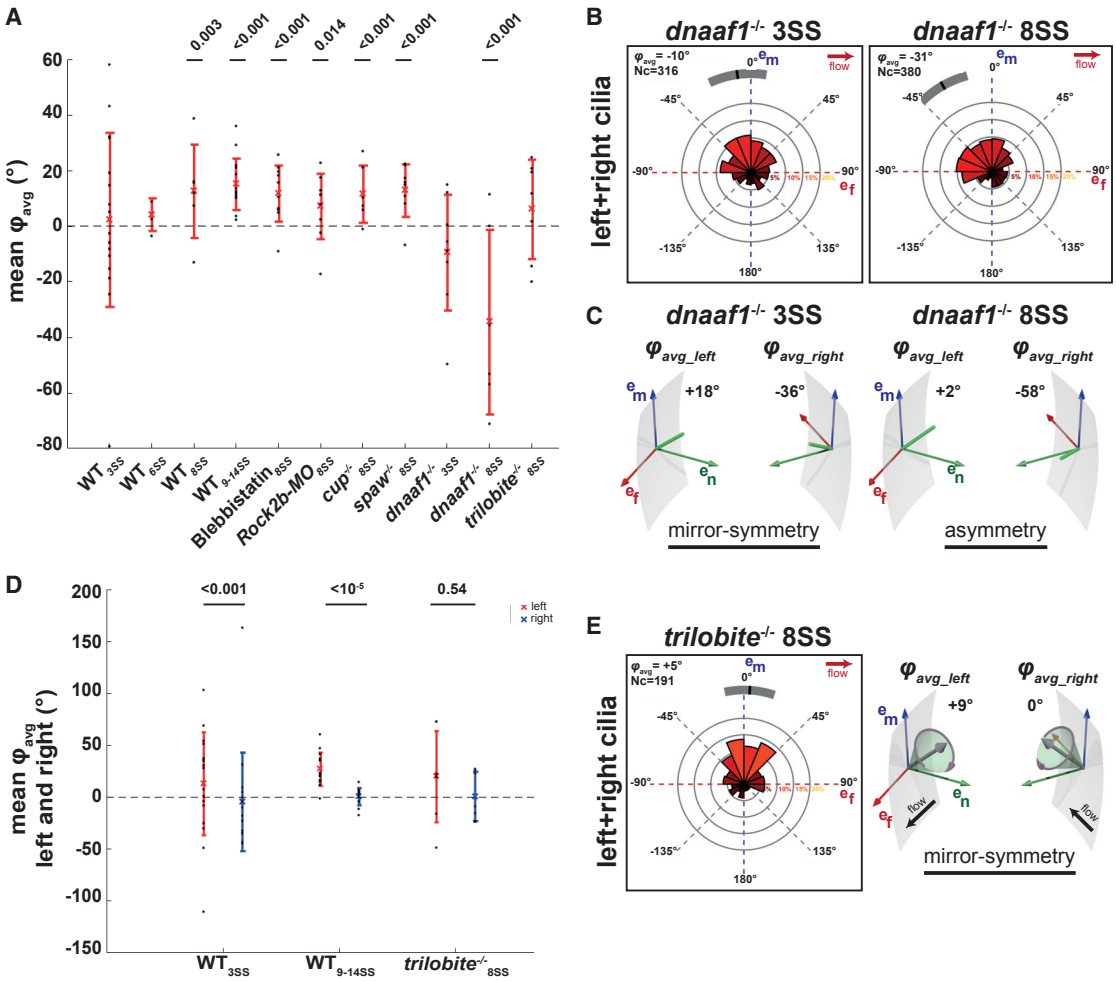

Figure 3. DNAAF1 and PCP Are Important for Asymmetric Cilia Orientation

(A) Mean orientations (φ_{avg}) for each condition. Each dot represents the mean for one KV, the cross indicates the average for all KVs, and the line indicates the SD. The mean values of φ_{avg} are always positive, except for *dnaaf1*$^{-/-}$, revealing that its orientation is reversed with respect to the meridional direction. WT3SS, WT6SS, *dnaaf1*$^{-/-}$3SS, and *trilobite*$^{-/-}$8SS have values close to zero, implying a symmetric KV.

(B) φ angle distribution of cilia in both KV hemispheres (left and right cilia), for *dnaaf1*$^{-/-}$3SS (upper) and *dnaaf1*$^{-/-}$8SS (lower). *dnaaf1*$^{-/-}$3SS and *dnaaf1*$^{-/-}$8SS cilia are inclined in the direction opposite to the flow (e_f).

(C) φ_{avg} on the left and right sides of the KV for *dnaaf1*$^{-/-}$3SS and *dnaaf1*$^{-/-}$8SS.

(D) Mean values of φ_{avg} on the left (red) and right (blue) sides of the KV for WT3SS, WT9-14SS, and *trilobite*$^{-/-}$8SS.

(E) φ angle distribution of cilia in both KV hemispheres (left and right cilia) and φ_{avg} (left/right) for *trilobite*$^{-/-}$8SS.

See also Figures S1 and S2 and Video S1.

orientation was perturbed (Figure S2A). We next studied *dnaaf1*$^{-/-}$ mutants. *dnaaf1* encodes for a cilium-specific protein that is required for ciliary architecture stability and cilia motility (Sullivan-Brown et al., 2008). *dnaaf1*$^{-/-}$ cilia have ultrastructural defects and display abnormal dynein arms orientation in beating cilia (Loges et al., 2009). All *dnaaf1*$^{-/-}$ cilia are immotile (Video S1), and embryos have randomized LR axes (Figures S4B and S4C; Table S2). We assessed cilia symmetry in the *dnaaf1*$^{-/-}$ and found no sign of asymmetry at 3SS ($\varphi_{avg\_left} \approx -\varphi_{avg\_right}$) ($\varphi_{avg} \approx 0°$ in Figure 3A; Figures 3B and 3C; Table S1), like controls (Figures 2 and S2B). At 8SS, *dnaaf1*$^{-/-}$ cilia orientation is asymmetric (Figures 3A–3C; Table S1), showing that asymmetric cilia orientation is flow independent. We were surprised to find that *dnaaf1*$^{-/-}$ cilia are inclined with a sinistral direction, which is opposite that of WT (Figures 3A, 3B, and S2A); $p < 10^{-5}$). Thus, *dnaaf1* is required for chiral cilia orientation independent of flow.

Since cilia motility and PCP are interdependent (Jaffe et al., 2016), we directly tested the role of the PCP in KV chirality. The PCP pathway modulates cilia tilt in the mouse LRO (Hashimoto and Hamada, 2010; Marshall and Kintner, 2008; Song et al., 2010). Generically speaking, PCP proteins establish cell polarity within tissues across a large variety of animal tissues (Wallingford, 2012). We used trilobite mutant, in which the protein essential for PCP signaling, Van gogh-like 2 (Vangl2), is mutated (Jessen and Solnica-Krezel, 2004). Vangl2 is required for KV cilia posterior tilt and LR determination (Borovina

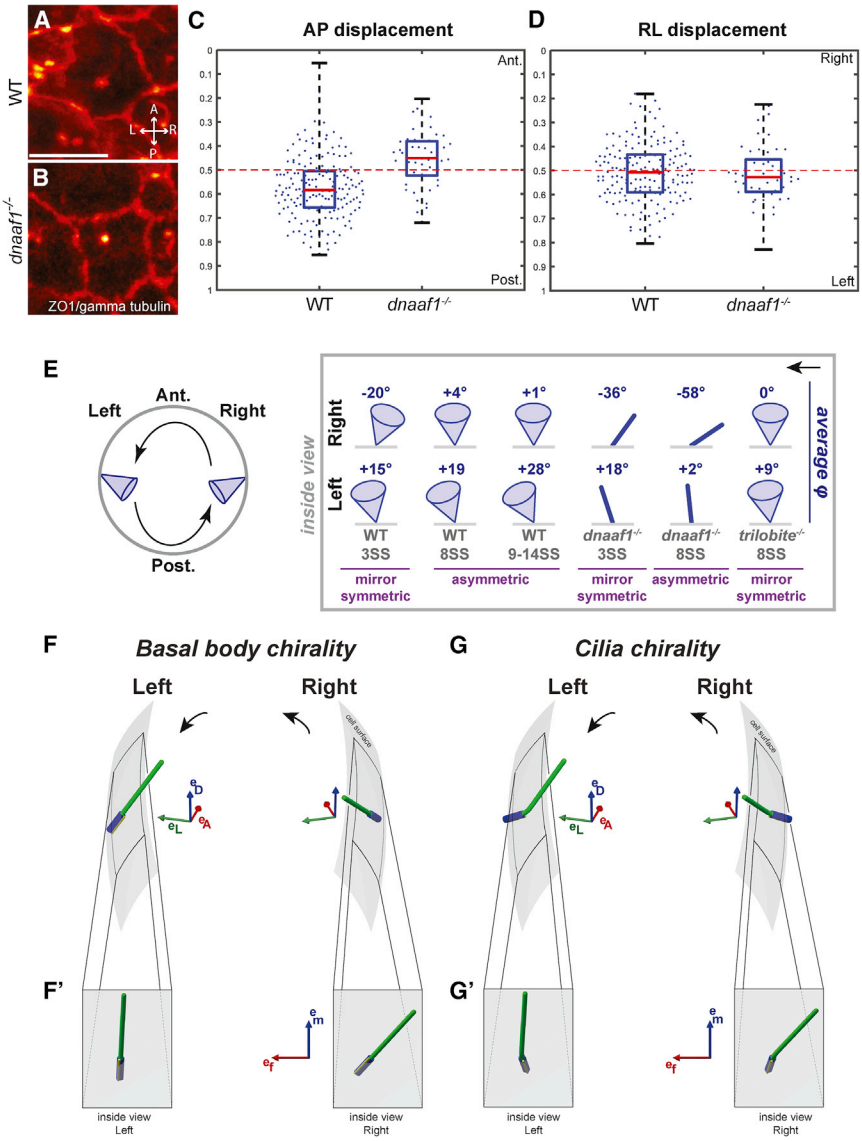

Figure 4. Basal Body Position in KV Cells, and Schematic Summary of the Contributions of Different Pathways and Potential Origins of Chirality Leading to Asymmetric Cilia Orientation in the KV

(A–D) Basal body position analysis. The positions of basal bodies relative to the AP or LR extension of each cell were extracted from WT (A) or *dnaaf1*$^{-/-}$ embryos (B) using an orthogonal projection of the fluorescence intensity on the plane tangential to the KV surface after ZO1 and gamma tubulin staining of KV cells. The distributions of AP displacements (0 = anterior, 1 = posterior) in (C) and LR displacements (0 = right, 1 = left) in (D) are centered in the middle of the cell (displacement at 0.5) for all of the cases, except for a posterior displacement of basal bodies in WT.

(E) Left, dorsal view of a mirror-symmetric KV showing a representative cilium on each side. Right, average φ orientation over time in WT, *dnaaf1*$^{-/-}$, and *trilobite*$^{-/-}$ KV for cilia in the right (upper row) and left (lower row) KV hemispheres. KV is mirror symmetric at 3SS in both WT and *dnaaf1*$^{-/-}$ embryos, evolving to an asymmetric orientation at 8SS. In contrast, *trilobite*$^{-/-}$ 8SS KVs do not show any asymmetry.

(F and G) Two hypotheses for the observed chirality (dorsal-posterior views of the KV in F and G, inside views of both sides in F' and G'): (F) cilia orientation can be asymmetric between left and right due to chiral orientation of the basal bodies; (G) alternatively, the basal bodies can be arranged symmetrically, but the chiral structure of each cilium leads to an overall asymmetric distribution of cilia orientations. Black arrows in (E), (F), and (G) indicate the flow direction.

See also Figures S3 and S4 and Video S1.

et al., 2010). We studied cilia orientation at 8SS using *trilobite;actb2:Mmu.Arl13b-GFP* (Heisenberg and Nüsslein-Volhard, 1997). These mutants display LR defects (Figures S4B and S4C; Table S2), but maintain cilia meridional tilt (Figures 3E and S1A). Simulations (see STAR Methods; Figure S4D) predict that flow is significantly weaker in *trilobite*$^{-/-}$ than in the WT ($p = 0.024$), as expected for PCP mutants (Borovina et al., 2010). However, we could not detect any asymmetry in the *trilobite*$^{-/-}$ KV cilia at 8SS ($p = 0.54$; Figures 3D, 3E, and S2C; Table S2) and $\varphi_{avg} \approx 0^{\circ}$ (Figure 3A). These results indicate that the PCP pathway controls chiral cilia orientation.

Because PCP controls the basal body position of cells (Borovina et al., 2010; Hashimoto and Hamada, 2010; Juan et al., 2018; Song et al., 2010), we quantified cilia basal body orientations to test whether both are interdependent (Figures S3B and S3C). As expected, the basal body localized in the posterior part of the cell (Figures 4A, 4C, and 4D). In *dnaaf1*$^{-/-}$, the basal body positions more centrally along the anterior-posterior (AP) axis (Figures 4A–4D), which is consistent with the fact that Dnaaf1/Lrrc50 interacts physically with C21orf59, a factor involved in polarizing motile cilia (Jaffe et al., 2016). By contrast, we did not detect any LR asymmetry of basal body positions in controls and mutants ($p > 0.15$ for both). Thus, chiral cilia orientation is not dependent on basal body position along the LR axis of the cells, which more generally suggests that cilia orientation is not solely controlled by basal body position. These results also show that *dnaaf1* sets the AP basal position and that cells may need to be planar polarized for the establishment of chiral cilia orientation. We conclude from this that cilia position and asymmetric orientation may be interdependent.

DISCUSSION

Previous work has focused on identifying signals that specify the left embryonic side in response to flow, but the chirality of the LRO remained untested. We studied the zebrafish KV and showed that cilia orientation is not symmetrical between the left and right sides. Our study revealed that cilia orientation

progressively changes from mirror symmetric to asymmetric (Figure 4E) and that the asymmetry emerges independently of the LR determination cascade. Despite a great variability in cilia orientation, we found that they will invariably become chiral in every KV, suggesting a robust process for chirality determination. However, the impact of the uncovered chirality on LR symmetry breaking remains to be determined.

Considering that key modulators of symmetry breaking such as Pkd2, Rock2b (and the associated actomyosin pathway), or Spaw do not affect asymmetric cilia orientation, we conclude that the LRO promotes LR symmetry breaking and asymmetric cilia orientation through distinct mechanisms. If the asymmetry of cilia orientation is independent of the LR machinery, then how can we explain its emergence? One possibility is that cilia reorient themselves in response to the flow, which would be the source of chiral information. During blood vessel formation, endothelial cells polarize against flow in a similar way (Franco et al., 2015; Kwon et al., 2016). There are, however, three strong arguments opposing this hypothesis. First, we still observe an asymmetric orientation of cilia in *dnaaf1*$^{-/-}$, where flow is absent and in *rock2b* MO, where flow is weak. Second, our previous work (Ferreira et al., 2017) along with simulations (Figure S4E) show that the torque resulting from the global flow is much smaller than the drag on a motile cilium. Similar conclusions were made when comparing the forces exerted by beating ependymal cilia with those mediated by the fluid (Mahuzier et al., 2018). Third, we found that the left cilia reorient less than the right cilia, even though the flow has the same magnitude on both sides (Ferreira et al., 2017). Thus, the relation between flow direction and cilia orientations cannot be causal. It is more likely that both reflect disorders in cilia orientation in the respective mutants.

We propose that the asymmetry arises from chiral influences generated by the cytoskeletal components (Satir, 2016). Accordingly, cells can display chiral behaviors *in vitro* and *in vivo* independently of an LRO (Naganathan et al., 2014; Noël et al., 2013; Spéder et al., 2006; Tee et al., 2015; Wan et al., 2016). For example, basal body and cilia ultrastructure display obvious signs of chirality (Afzelius, 1976; Marshall, 2012; Pearson, 2014). This suggests two possibilities: either orientation of the cilia basal bodies is asymmetric between left and right (Figures 4F and 4F') or they are oriented symmetrically, and the intrinsic chiral structure of each cilium leads to asymmetric cilia orientations (Figures 4G and 4G'). The fact that Dnaaf1 loss reverses cilia orientation from dextral to sinistral seems to argue for the latter. However, we found that Dnaaf1 is also involved in modulating PCP, making its function within the cilium difficult to assess. The basal body position is not chiral. This suggests that chirality relates to basal body orientation but not its position. An attractive hypothesis is that cells need to be planar cell polarized to express chirality and that the PCP participates in the process setting basal body orientation through Vangl2 and Dnaaf1. Among the many PCP components that affect LR determination, from ciliary components (Jaffe et al., 2016) to unconventional Myosin 1d (Juan et al., 2018; Tingler et al., 2018), it will be interesting to assess their involvement in controlling cilia chirality and its robustness.

The demonstration that the asymmetry is actively modulated by the PCP, cilia motility, and, potentially, the internal organization of cilia has important implications for understanding chiral information distribution and control in developing organs. It shows that chiral information is dynamic and temporally controlled during the course of LR specification. In that respect, it is interesting that cells establish chiral organization as a result of cell migration *in vitro* (Wan et al., 2011) and that asymmetric cell migration occurs in the chicken LRO (Gros et al., 2009). Thus, the progressive establishment of asymmetric cilia orientation may reflect an active acquisition of cellular chirality during the time of LRO function. If confirmed, then chirality would represent a unique conserved feature between fish and chicken LRO. This raises the intriguing possibility of a more general role for chirality in morphogenetic pattern formation and LR symmetry breaking. Could the chiral cilia orientation participate in symmetry breaking in the LRO? We have previously tested different hypothetical mechanisms of flow detection and shown that a quantitative analysis of physical limits favors chemical sensing (Ferreira et al., 2017). While the basic mechanisms of flow generation and flow detection do not require any prior asymmetry in the KV, it is possible that the ciliary asymmetry participates in the process of symmetry breaking by working hand in hand with the chiral flow to optimize the flow direction or the detection of signaling particles.

More generally, proper cilia orientation is essential for flow generation in ciliated tissues or for the swimming of ciliated microorganisms (Goldstein, 2015). It is still unclear whether cilia can reorient themselves in the direction of flow (Guirao et al., 2010; Mitchell, 2003) and whether this reorientation is a consequence of hydrodynamic forces. Another possibility is that cell polarity is affected by the flow. Because some ciliary proteins involved in cilia motility also participate in PCP (Jaffe et al., 2016), the spatial orientation of motile cilia could be an intrinsic property, independent of the flow they generate. In brain cavities, the orientation of cilia beating dynamically follows the circadian rhythm and may be driven by transient changes in cell-cell interactions and PCP (Faubel et al., 2016). Similarly, microorganisms can reorient the ciliary beat as an avoidance reaction (Tamm et al., 1975). Mechanical strain also dictates cilia orientation (Chien et al., 2018). Our study sheds a different light on these systems, as it shows that cilia orientation is related to cell polarity in a complex way that includes an intrinsic sense of chirality. Considering that congenital diseases such as idiopathic scoliosis (Grimes et al., 2016), Kartagener syndrome, neonatal respiratory distress, hydrocephaly, and male infertility involve cilia motility (Mitchison and Valente, 2017), precise cilia orientation analysis becomes critical to understanding the biological principles that govern cilia function and their potential involvement in pathology. In this context, our conclusions and method could be relevant in the study of a variety of developing organs.

STAR★METHODS

Detailed methods are provided in the online version of this paper and include the following:

- KEY RESOURCES TABLE
- CONTACT FOR REAGENT AND RESOURCE SHARING

SUPPLEMENTAL INFORMATION

Supplemental Information includes four figures, three tables, one video, and one data file and can be found with this article online at https://doi.org/10.1016/j.celrep.2018.10.069.

ACKNOWLEDGMENTS

We thank C. Norden, M. Blum, M. Fürthauer, and the Vermot lab for discussion and thoughtful comments on the manuscript—in particular, R. Chow for help with editing. We also thank the Heisenberg lab for sharing the *trilobite* line. This work was supported by the FRM (DEQ20140329553); the ANR (ANR-15-CE13-0015-01, ANR-12-ISV2-0001-01, and ANR-11-EQPX-0029); the EMBO Young Investigator Program; the European Community; the ERC (CoG no. 682938 Evalve and grant no. ANR-10-LABX-0030-INRT); and a French state fund managed by the Agence Nationale de la Recherche under the frame program Investissements d'Avenir (ANR-10-IDEX-0002-02). R.R.F. was supported by the IGBMC International PhD program (LABEX, Laboratory of Excellence). G.P. was supported by the Interdisciplinary Initiative (IDI) from IDEX (Initiative of Excellence) Paris-Saclay (IDI PhD program). H.F. was supported by the USIAS (grant no. USIAS-2017-097). A.V. acknowledges support from the Slovenian Research Agency (grant no. P1-0099).

AUTHOR CONTRIBUTIONS

Conceptualization, A.V., W.S., and J.V. Visualization, R.R.F. and A.V. Methodology, A.V., G.P., and W.S. Resources, J.V. Data Curation, R.R.F., H.F., L.K., and J.V. Investigation, R.R.F., A.V., W.S., and J.V. Software, G.P. Formal Analysis, R.R.F., A.V., G.P., and W.S. Validation, A.V. and J.V. Writing – Original Draft, A.V., W.S., and J.V. Writing – Review & Editing, R.R.F., A.V., W.S., and J.V. Funding Acquisition, A.V., W.S., and J.V. Supervision, W.S. and J.V. Project Administration, J.V.

DECLARATION OF INTERESTS

The authors declare no competing interests.

Received: January 8, 2018
Revised: September 13, 2018
Accepted: October 18, 2018
Published: November 20, 2018

REFERENCES

Afzelius, B.A. (1976). A human syndrome caused by immotile cilia. Science *193*, 317–319.

Blum, M., Schweickert, A., Vick, P., Wright, C.V., and Danilchik, M.V. (2014a). Symmetry breakage in the vertebrate embryo: when does it happen and how does it work? Dev. Biol. *393*, 109–123.

Blum, M., Feistel, K., Thumberger, T., and Schweickert, A. (2014b). The evolution and conservation of left-right patterning mechanisms. Development *141*, 1603–1613.

Borovina, A., Superina, S., Voskas, D., and Ciruna, B. (2010). Vangl2 directs the posterior tilting and asymmetric localization of motile primary cilia. Nat. Cell Biol. *12*, 407–412.

Chien, Y.H., Srinivasan, S., Keller, R., and Kintner, C. (2018). Mechanical strain determines cilia length, motility, and planar position in the left-right organizer. Dev. Cell *45*, 316–330.e4.

Coutelis, J.B., González-Morales, N., Géminard, C., and Noselli, S. (2014). Diversity and convergence in the mechanisms establishing L/R asymmetry in metazoa. EMBO Rep. *15*, 926–937.

Dasgupta, A., and Amack, J.D. (2016). Cilia in vertebrate left-right patterning. Philos. Trans. R. Soc. Lond. B Biol. Sci. *371*, 20150410.

Davison, A., McDowell, G.S., Holden, J.M., Johnson, H.F., Koutsovoulos, G.D., Liu, M.M., Hulpiau, P., Van Roy, F., Wade, C.M., Banerjee, R., et al. (2016). Formin is associated with left-right asymmetry in the pond snail and the frog. Curr. Biol. *26*, 654–660.

Essner, J.J., Amack, J.D., Nyholm, M.K., Harris, E.B., and Yost, H.J. (2005). Kupffer's vesicle is a ciliated organ of asymmetry in the zebrafish embryo that initiates left-right development of the brain, heart and gut. Development *132*, 1247–1260.

Faubel, R., Westendorf, C., Bodenschatz, E., and Eichele, G. (2016). Cilia-based flow network in the brain ventricles. Science *353*, 176–178.

Ferreira, R.R., and Vermot, J. (2016). The balancing roles of mechanical forces during left-right patterning and asymmetric morphogenesis. Mech. Dev. *144*, 71–80.

Ferreira, R.R., Vilfan, A., Jülicher, F., Supatto, W., and Vermot, J. (2017). Physical limits of flow sensing in the left-right organizer. eLife *6*, e25078.

Fliegauf, M., Benzing, T., and Omran, H. (2007). When cilia go bad: cilia defects and ciliopathies. Nat Rev Mol Cell Biol. *8*, 880–893.

Francescatto, L., Rothschild, S.C., Myers, A.L., and Tombes, R.M. (2010). The activation of membrane targeted CaMK-II in the zebrafish Kupffer's vesicle is required for left-right asymmetry. Development *137*, 2753–2762.

Franco, C.A., Jones, M.L., Bernabeu, M.O., Geudens, I., Mathivet, T., Rosa, A., Lopes, F.M., Lima, A.P., Ragab, A., Collins, R.T., et al. (2015). Dynamic endothelial cell rearrangements drive developmental vessel regression. PLoS Biol *13*, e1002125.

Freund, J.B., Goetz, J.G., Hill, K.L., and Vermot, J. (2012). Fluid flows and forces in development: functions, features and biophysical principles. Development *139*, 1229–1245.

Goldstein, R.E. (2015). Green Algae as Model Organisms for Biological Fluid Dynamics. Annu Rev Fluid Mech *47*, 343–375.

Gómez-López, S., Lerner, R.G., and Petritsch, C. (2014). Asymmetric cell division of stem and progenitor cells during homeostasis and cancer. Cell. Mol. Life Sci. *71*, 575–597.

Grimes, D.T., Boswell, C.W., Morante, N.F., Henkelman, R.M., Burdine, R.D., and Ciruna, B. (2016). Zebrafish models of idiopathic scoliosis link cerebrospinal fluid flow defects to spine curvature. Science *352*, 1341–1344.

Gros, J., Feistel, K., Viebahn, C., Blum, M., and Tabin, C.J. (2009). Cell movements at Hensen's node establish left/right asymmetric gene expression in the chick. Science *324*, 941–944.

Guirao, B., Meunier, A., Mortaud, S., Aguilar, A., Corsi, J.M., Strehl, L., Hirota, Y., Desoeuvre, A., Boutin, C., Han, Y.G., et al. (2010). Coupling between hydrodynamic forces and planar cell polarity orients mammalian motile cilia. Nat. Cell Biol. *12*, 341–350.

Hamada, H., and Tam, P.P. (2014). Mechanisms of left-right asymmetry and patterning: driver, mediator and responder. F1000Prime Rep. *6*, 110.

Hashimoto, M., and Hamada, H. (2010). Translation of anterior-posterior polarity into left-right polarity in the mouse embryo. Curr. Opin. Genet. Dev. *20*, 433–437.

Heisenberg, C.P., and Nüsslein-Volhard, C. (1997). The function of silberblick in the positioning of the eye anlage in the zebrafish embryo. Dev. Biol. *184*, 85–94.

Hesterberg, T., Moore, D.S., Monaghan, S., Clipson, A., Epstein, R., and McCabe, G.P. (2005). Bootstrap methods and permutation tests. In Introduction to the Practice of Statistics, Fifth Edition, W.H. McCabe, ed. (Freeman & Co.), pp. 14.1–14.70.

Hilfinger, A., and Jülicher, F. (2008). The chirality of ciliary beats. Phys. Biol. *5*, 016003.

Hong, H., Kim, J., and Kim, J. (2015). Myosin heavy chain 10 (MYH10) is required for centriole migration during the biogenesis of primary cilia. Biochem. Biophys. Res. Commun. *461*, 180–185.

Hozumi, S., Maeda, R., Taniguchi, K., Kanai, M., Shirakabe, S., Sasamura, T., Spéder, P., Noselli, S., Aigaki, T., Murakami, R., and Matsuno, K. (2006). An unconventional myosin in Drosophila reverses the default handedness in visceral organs. Nature *440*, 798–802.

Inaki, M., Sasamura, T., and Matsuno, K. (2018). Cell Chirality Drives Left-Right Asymmetric Morphogenesis. Front. Cell Dev. Biol. *6*, 34.

Jaffe, K.M., Grimes, D.T., Schottenfeld-Roames, J., Werner, M.E., Ku, T.S., Kim, S.K., Pelliccia, J.L., Morante, N.F., Mitchell, B.J., and Burdine, R.D. (2016). c21orf59/kurly controls both cilia motility and polarization. Cell Rep. *14*, 1841–1849.

Jessen, J.R., and Solnica-Krezel, L. (2004). Identification and developmental expression pattern of van gogh-like 1, a second zebrafish strabismus homologue. Gene Expr. Patterns *4*, 339–344.

Juan, T., Géminard, C., Coutelis, J.B., Cerezo, D., Polès, S., Noselli, S., and Fürthauer, M. (2018). Myosin1D is an evolutionarily conserved regulator of animal left-right asymmetry. Nat. Commun. *9*, 1942.

Kalogirou, S., Malissovas, N., Moro, E., Argenton, F., Stainier, D.Y., and Beis, D. (2014). Intracardiac flow dynamics regulate atrioventricular valve morphogenesis. Cardiovasc. Res. *104*, 49–60.

Kramer-Zucker, A.G., Olale, F., Haycraft, C.J., Yoder, B.K., Schier, A.F., and Drummond, I.A. (2005). Cilia-driven fluid flow in the zebrafish pronephros, brain and Kupffer's vesicle is required for normal organogenesis. Development *132*, 1907–1921.

Kuroda, R., Endo, B., Abe, M., and Shimizu, M. (2009). Chiral blastomere arrangement dictates zygotic left-right asymmetry pathway in snails. Nature *462*, 790–794.

Kwon, H.B., Wang, S., Helker, C.S., Rasouli, S.J., Maischein, H.M., Offermanns, S., Herzog, W., and Stainier, D.Y. (2016). In vivo modulation of endothelial polarization by Apelin receptor signalling. Nat Commun *7*, 11805.

Levin, M. (2005). Left-right asymmetry in embryonic development: a comprehensive review. Mech. Dev. *122*, 3–25.

Loges, N.T., Olbrich, H., Becker-Heck, A., Häffner, K., Heer, A., Reinhard, C., Schmidts, M., Kispert, A., Zariwala, M.A., Leigh, M.W., et al. (2009). Deletions and point mutations of LRRC50 cause primary ciliary dyskinesia due to dynein arm defects. Am. J. Hum. Genet. *85*, 883–889.

Long, S., Ahmad, N., and Rebagliati, M. (2003). The zebrafish nodal-related gene southpaw is required for visceral and diencephalic left-right asymmetry. Development *130*, 2303–2316.

Mahuzier, A., Shihavuddin, A., Fournier, C., Lansade, P., Faucourt, M., Menezes, N., Meunier, A., Garfa-Traoré, M., Carlier, M.F., Voituriez, R., et al. (2018). Ependymal cilia beating induces an actin network to protect centrioles against shear stress. Nat. Commun. *9*, 2279.

Marshall, W.F. (2012). Centriole asymmetry determines algal cell geometry. Curr Opin Plant Biol. *15*, 632–637.

Marshall, W.F., and Kintner, C. (2008). Cilia orientation and the fluid mechanics of development. Curr. Opin. Cell Biol. *20*, 48–52.

Mitchell, D.R. (2003). Orientation of the central pair complex during flagellar bend formation in Chlamydomonas. Cell Motil. Cytoskeleton *56*, 120–129.

Mitchison, H.M., and Valente, E.M. (2017). Motile and non-motile cilia in human pathology: from function to phenotypes. J. Pathol. *241*, 294–309.

Monteiro, R., van Dinther, M., Bakkers, J., Wilkinson, R., Patient, R., ten Dijke, P., and Mummery, C. (2008). Two novel type II receptors mediate BMP signalling and are required to establish left-right asymmetry in zebrafish. Dev. Biol. *315*, 55–71.

Morrow, S.M., Bissette, A.J., and Fletcher, S.P. (2017). Transmission of chirality through space and across length scales. Nat. Nanotechnol. *12*, 410–419.

Naganathan, S.R., Fürthauer, S., Nishikawa, M., Jülicher, F., and Grill, S.W. (2014). Active torque generation by the actomyosin cell cortex drives left-right symmetry breaking. eLife *3*, e04165.

Noël, E.S., Verhoeven, M., Lagendijk, A.K., Tessadori, F., Smith, K., Choorapoikayil, S., den Hertog, J., and Bakkers, J. (2013). A Nodal-independent and tissue-intrinsic mechanism controls heart-looping chirality. Nat. Commun. *4*, 2754.

Okada, Y., Takeda, S., Tanaka, Y., Belmonte, J.I., and Hirokawa, N. (2005). Mechanism of nodal flow: a conserved symmetry breaking event in left-right axis determination. Cell *121*, 633–644.

Pearson, C.G. (2014). Choosing sides–asymmetric centriole and basal body assembly. J Cell Sci.*127*, pp. 2803–2810.

Pitaval, A., Tseng, Q., Bornens, M., and Théry, M. (2010). Cell shape and contractility regulate ciliogenesis in cell cycle-arrested cells. J. Cell Biol. *191*, 303–312.

Qiu, D., Cheng, S.M., Wozniak, L., McSweeney, M., Perrone, E., and Levin, M. (2005). Localization and loss-of-function implicates ciliary proteins in early, cytoplasmic roles in left-right asymmetry. Dev. Dyn. *234*, 176–189.

Ramsdell, A.F. (2005). Left-right asymmetry and congenital cardiac defects: getting to the heart of the matter in vertebrate left-right axis determination. Dev. Biol. *288*, 1–20.

Sarmah, B., Latimer, A.J., Appel, B., and Wente, S.R. (2005). Inositol polyphosphates regulate zebrafish left-right asymmetry. Dev. Cell *9*, 133–145.

Satir, P. (2016). Chirality of the cytoskeleton in the origins of cellular asymmetry. Philos Trans R Soc Lond B Biol Sci. *371* (*1710*).

Sato, K., Hiraiwa, T., Maekawa, E., Isomura, A., Shibata, T., and Kuranaga, E. (2015). Left-right asymmetric cell intercalation drives directional collective cell movement in epithelial morphogenesis. Nat. Commun. *6*, 10074.

Schottenfeld, J., Sullivan-Brown, J., and Burdine, R.D. (2007). Zebrafish curly up encodes a Pkd2 ortholog that restricts left-side-specific expression of southpaw. Development *134*, 1605–1615.

Shapiro, A.J., Davis, S.D., Ferkol, T., Dell, S.D., Rosenfeld, M., Olivier, K.N., Sagel, S.D., Milla, C., Zariwala, M.A., Wolf, W., et al. (2014). Laterality defects other than situs inversus totalis in primary ciliary dyskinesia: insights into situs ambiguus and heterotaxy. Chest *146*, 1176–1186.

Shibazaki, Y., Shimizu, M., and Kuroda, R. (2004). Body handedness is directed by genetically determined cytoskeletal dynamics in the early embryo. Curr. Biol. *14*, 1462–1467.

Shinohara, K., and Hamada, H. (2017). Cilia in left-right symmetry breaking. Cold Spring Harb. Perspect. Biol. *9*, a028282.

Song, H., Hu, J., Chen, W., Elliott, G., Andre, P., Gao, B., and Yang, Y. (2010). Planar cell polarity breaks bilateral symmetry by controlling ciliary positioning. Nature *466*, 378–382.

Spéder, P., Adám, G., and Noselli, S. (2006). Type ID unconventional myosin controls left-right asymmetry in Drosophila. Nature *440*, 803–807.

Sullivan-Brown, J., Schottenfeld, J., Okabe, N., Hostetter, C.L., Serluca, F.C., Thiberge, S.Y., and Burdine, R.D. (2008). Zebrafish mutations affecting cilia motility share similar cystic phenotypes and suggest a mechanism of cyst formation that differs from pkd2 morphants. Dev. Biol. *314*, 261–275.

Supatto, W., Fraser, S.E., and Vermot, J. (2008). An all-optical approach for probing microscopic flows in living embryos. Biophys. J. *95*, L29–L31.

Supatto, W., and Vermot, J. (2011). From cilia hydrodynamics to zebrafish embryonic development. Curr. Top. Dev. Biol. *95*, 33–66.

Sutherland, M.J., and Ware, S.M. (2009). Disorders of left-right asymmetry: heterotaxy and situs inversus. Am J Med Genet C Semin Med Genet. *151C*, 307–317.

Taber, L.A. (2006). Biophysical mechanisms of cardiac looping. Int. J. Dev. Biol. *50*, 323–332.

Tabin, C.J., and Vogan, K.J. (2003). A two-cilia model for vertebrate left-right axis specification. Genes Dev. *17*, 1–6.

Tamm, S.L., Sonneborn, T.M., and Dippell, R.V. (1975). The role of cortical orientation in the control of the direction of ciliary beat in Paramecium. J. Cell Biol. *64*, 98–112.

Tee, Y.H., Shemesh, T., Thiagarajan, V., Hariadi, R.F., Anderson, K.L., Page, C., Volkmann, N., Hanein, D., Sivaramakrishnan, S., Kozlov, M.M., and Bershadsky, A.D. (2015). Cellular chirality arising from the self-organization of the actin cytoskeleton. Nat. Cell Biol. *17*, 445–457.

Thisse, C., and Thisse, B. (2008). High-resolution in situ hybridization to whole-mount zebrafish embryos. Nat. Protoc. *3*, 59–69.

Tingler, M., Kurz, S., Maerker, M., Ott, T., Fuhl, F., Schweickert, A., LeBlanc-Straceski, J.M., Noselli, S., and Blum, M. (2018). A conserved role of the unconventional myosin 1d in laterality determination. Curr. Biol. *28*, 810–816.e3.

Vandenberg, L.N., and Levin, M. (2013). A unified model for left-right asymmetry? Comparison and synthesis of molecular models of embryonic laterality. Dev. Biol. *379*, 1–15.

Wagnière, G.H. (2007). On Chirality and the Universal Asymmetry: Reflections on Image and Mirror Image (Wiley-VCH).

Wallingford, J.B. (2012). Planar cell polarity and the developmental control of cell behavior in vertebrate embryos. Annu. Rev. Cell Dev. Biol. *28*, 627–653.

Wan, L.Q., Chin, A.S., Worley, K.E., and Ray, P. (2016). Cell chirality: emergence of asymmetry from cell culture. Philos. Trans. R. Soc. Lond. B Biol. Sci. *371*, 371.

Wan, L.Q., Ronaldson, K., Park, M., Taylor, G., Zhang, Y., Gimble, J.M., and Vunjak-Novakovic, G. (2011). Micropatterned mammalian cells exhibit phenotype-specific left-right asymmetry. Proc. Natl. Acad. Sci. USA *108*, 12295–12300.

Wang, G., Cadwallader, A.B., Jang, D.S., Tsang, M., Yost, H.J., and Amack, J.D. (2011). The Rho kinase Rock2b establishes anteroposterior asymmetry of the ciliated Kupffer's vesicle in zebrafish. Development *138*, 45–54.

Wang, G., Manning, M.L., and Amack, J.D. (2012). Regional cell shape changes control form and function of Kupffer's vesicle in the zebrafish embryo. Dev. Biol. *370*, 52–62.

Xu, J., Van Keymeulen, A., Wakida, N.M., Carlton, P., Berns, M.W., and Bourne, H.R. (2007). Polarity reveals intrinsic cell chirality. Proc. Natl. Acad. Sci. USA *104*, 9296–9300.

Yuan, S., Zhao, L., Brueckner, M., and Sun, Z. (2015). Intraciliary calcium oscillations initiate vertebrate left-right asymmetry. Curr. Biol. *25*, 556–567.

STAR★METHODS

KEY RESOURCES TABLE

REAGENT or RESOURCE	SOURCE	IDENTIFIER
Antibodies		
Mouse monoclonal ZO1	Thermo Fisher Scientific	Cat. #33-9100; RRID: AB_2533147
Mouse monoclonal gamma tubulin	Sigma-Aldrich	Cat. #T6557; RRID: AB_477584
Mouse Alexa Fluor 546 IgG	Thermo Fisher Scientific	Cat. #A-11030; RRID: AB_144695
Chemicals, Peptides, and Recombinant Proteins		
Tricaine/MS-222	Sigma-Aldrich	Cat. # A-5040
Blebbistatin	Sigma-Aldrich	Cat. # B0560; CAS: 856925-71-8
DMSO	Sigma-Aldrich	Cat. # D8418; CAS: 67-68-5
Bodipy TR Ceramide	ThermoFisher Scientific	Cat. # D7540
UltraPure Low Melting Point Agarose	ThermoFisher Scientific	Cat. # 16520050
Formaldehyde	Sigma-Aldrich	Cat. # F8775; CAS: 50-00-0
MOPS	Sigma-Aldrich	Cat. # M1254; CAS: 1132-61-2
EGTA	Sigma-Aldrich	Cat. # E3889; CAS: 67-42-5
$MgSO_4$	VWR Chemicals	Cat. # 470301-688; CAS: 7487-88-9
PBS 10X	ThermoFisher Scientific	Cat. # SH3001302
Bovine Serum Albumin (BSA)	H2B	Cat. # 1005-70; CAS: 9048-46-8
Triton X-100	Sigma-Aldrich	Cat. # T8787; CAS: 9002-93-1
Methanol	VWR Chemicals	Cat. # 1.06012.2500; CAS: 67-56-1
Experimental Models: Organisms/Strains		
Zebrafish: *actb2:*Mmu.*Arl13b-GFP*	Borovina et al., 2010	ZFIN ID: ZDB-TGCONSTRCT-100721-1
Zebrafish: *dnaaf1^{tm317b}; actb2:*Mmu.*Arl13b-GFP*	Sullivan-Brown et al., 2008	ZFIN ID: ZDB-FISH-150901-13987
Zebrafish: *trilobite^{tc240a}; actb2:*Mmu.*Arl13b-GFP*	Heisenberg and Nüsslein-Volhard, 1997	ZFIN ID: ZDB-FISH-150901-29686
Zebrafish: *spaw^{s457}; actb2:*Mmu.*Arl13b-GFP*	Kalogirou et al., 2014	ZFIN ID: ZDB-FISH-150901-2971
Zebrafish: *cup^{tc321}; actb2:Arl13b-GFP*	Schottenfeld et al., 2007	ZFIN ID: ZDB-FISH-150901-2453
Oligonucleotides		
Morpholino: *rock2b*-MO 5′-GCACACACTCACTCA CCAGCTGCAC-3′	Wang et al., 2011 Gene Tools	ZFIN ID: ZDB-MRPHLNO-110119-3
Digoxigenin RNA probe: *spaw*	Long et al., 2003	N/A
Digoxigenin RNA probe: *foxA3*	Monteiro et al., 2008	N/A
Primers for dnaaf1tm317b, see Table S3	This paper	N/A
Primers for cuptc321, see Table S3	This paper	N/A
Primers for spaws457, see Table S3	This paper	N/A
Software and Algorithms		
ApE- A plasmid Editor	M. Wayne Davis	http://jorgensen.biology.utah.edu/wayned/ape/
Imaris	Bitplane	RRID: SCR_007370
MATLAB	The MathWorks	RRID: SCR_001622
Microsoft Excel	Microsoft	Version 14.4.8

CONTACT FOR REAGENT AND RESOURCE SHARING

Further information and requests for reagents may be directed to, and will be fulfilled by the Lead Contact Julien Vermot (julien@igbmc.fr).

EXPERIMENTAL MODEL AND SUBJECT DETAILS

Zebrafish

Animal experiments were approved by the Animal Experimentation Committee of the Institutional Review Board of the IGBMC. The zebrafish (*Danio rerio*) lines used in this study were the following: *Tg*(*actb2:*Mmu.*Arl13b-GFP*) (Borovina et al., 2010), *Tg*(*dnaaf1*^{tm317b}*; actb2:*Mmu.*Arl13b-GFP*) (Sullivan-Brown et al., 2008), *Tg*(*trilobite*^{tc240a}*; actb2:*Mmu.*Arl13b-GFP*) (Heisenberg and Nüsslein-Volhard, 1997), *Tg*(*spaw*^{s457}*; actb2:*Mmu.*Arl13b-GFP*) (Kalogirou et al., 2014), *Tg*(*cup*^{tc241}*; actb2:Arl13b-GFP*) (Schottenfeld et al., 2007). None of the mutant lines display cilia length or KV shape defects (Figures S1B and S1C). All zebrafish strains were maintained at the IGBMC fish facility under standard husbandry conditions (14h light/10h dark cycle). Adult fish were anaesthetized with 80 μg/mL Tricaine/MS-222 for genotyping experiments. All primers used for the genotyping of the mutant lines were designed with the program ApE (http://jorgensen.biology.utah.edu/wayned/ape/) and using the genomic sequences available on Ensembl (*Ensembl genome browser 84*) for *dnaaf1, spaw* and *cup* genes. Embryos from the *trilobite*^{tc240a} (Heisenberg and Nüsslein-Volhard, 1997) mutant line were identifiable by phenotype at all stages analyzed. Mutant embryos from the *dnaaf1*^{tm317b} (Sullivan-Brown et al., 2008) *and cup*^{tc241} (Schottenfeld et al., 2007) were identifiable for heart and gut scoring analysis (48-53 hpf) and needed to be genotyped by sequencing only at earlier stages. *spaw*^{s457} (Kalogirou et al., 2014) mutant embryos were always genotyped by sequencing.

METHOD DETAILS

Morpholino (MO) knockdown

MOs designed to block the *rock2b* RNA splicing site (Wang et al., 2011) and the *dnah9* (*lrdr1)* translation start codon were obtained from *Gene Tools, LLC*. One-cell stage embryos were injected with 0.66ng of *rock2b*-MO (Essner et al., 2005) (5′-GCACA CACTCACTCACCAGCTGCAC-3′) and 2ng of *dnah9*-MO (5′-GCGGTTCCTGCTCCTCCATCGCGCC-3′).

Blebbistatin treatment

Embryos were dechorionated and treated with 35 μM of Blebbistatin (SIGMA B0560/DMSO) from bud-stage until 3-somite stage (SS) when they were washed in 0.3% Danieau medium and kept at 32°C until the desired stage for live imaging (8SS). 1%-DMSO treated embryos were used to monitor potential drug-control effects.

2-photon excited fluorescence (2PEF) microscopy

Live imaging experiments were performed as described in (Ferreira et al., 2017), in order to maximize the scanning artifact that allows to properly reconstruct cilia orientation in 3D as described in (Supatto and Vermot, 2011). Thus, zebrafish embryos were raised at 32°C in the dark and soaked in with Bodipy TR (Molecular Probes) for 60 min prior to the desired developmental stage. Embryos were subsequently embedded in 0.8% low melting point agarose in Danieau solution and imaged between 3- and 14-SS.

Briefly, each embryo was imaged using 2PEF microscopy with a TCP SP5 or SP8 direct microscope (Leica Inc.) at 930 nm wavelength (Chameleon Ultra laser, Coherent Inc.) using a water immersion objective (Leica, 25x, 0.95 NA). We imaged the KV of embryos labeled with both Arl13b-GFP and Bodipy TR between 3- and 14-SS: 100 × 100 × 50 μm^3 3D-stacks with 0.2 × 0.2 × 0.8 μm^3 voxel size and 2.4 μs pixel dwell time as described in (Ferreira et al., 2017). The fluorescence signal was collected using hybrid internal detectors at 493–575 nm and 594–730 nm in order to discriminate the GFP signal labeling cilia from the Bodipy TR signal. To uncover the orientation of the KV within the body axes, the midline was also imaged. We typically imaged a volume of 600 × 600 × 150 μm^3 comprising the midline and the KV from top to bottom with a voxel size of 1.15 μm laterally and 5 μm axially.

3D-Cilia Map: quantitative 3D cilia feature mapping

We used *3D-Cilia Map*, a quantitative imaging strategy to visualize and quantify the 3D biophysical features of all endogenous cilia in the KV in live zebrafish embryos, such as KV size and shape and cilia density, orientation or motility. This image analysis workflow using Imaris (Bitplane Inc.) and custom-made scripts in MATLAB (The MathWorks Inc.) was first described in (Ferreira et al., 2017). We improved its automation to facilitate the analysis of a large number of cilia. In addition, we added a new quantification feature, such as the length of both motile and immotile cilia, which is estimated based on the radial fluorescence intensity profile originating from the position of each cilium basal body. All coordinate system definitions are described by (Ferreira et al., 2017). In particular, the cilium orientation is represented as a unit vector from its base to its tip, with angle θ and φ defined in a local basis (Figure 1B). This vector represents the orientation of the rotation axis of motile cilia or of the cilium body orientation in the case of immotile cilia, which are both obtained from experimental images. The average angles φ_{avg} and θ_{avg} used throughout this work describe the direction of the 3D resultant vector, which is the sum of all considered cilia unit vectors.

Whole-mount *in situ* hybridization (WISH)

Whole-mount *in situ* hybridization was performed as described previously (Thisse and Thisse, 2008). Digoxigenin RNA probes were synthesized from DNA templates of *spaw* (Long et al., 2003) and *foxA3* (Monteiro et al., 2008). Embryos for *spaw* and *foxA3* WISH were fixed at 17SS and 53 hours post fertilization (hpf) respectively. The zebrafish heart looping was assessed at 48hpf when the

heart is already beating. Due to its transparency, the heart loop can be visible using brightfield illumination. We performed WISH for *foxA3* at 53hpf in order to visualize the gut *situs* (Monteiro et al., 2008) in the same embryos in which we previously assessed the heart looping at 48hpf. Embryos were evaluated after WISH and scored according to the curvature between the liver and the pancreas. For the sake of simplicity, we merged the laterality information of both heart and gut and described it according to the clinical terminology: *situs solitus* (heart and gut with normal orientation), *situs inversus* (complete reversal of both organ laterality) and *heterotaxy* (any combination of abnormal LR asymmetries that cannot be strictly classified as *situs inversus*) (Fliegauf et al., 2007; Ramsdell, 2005; Shapiro et al., 2014; Sutherland and Ware, 2009). *Spaw* expression patterns in the lateral plate mesoderm can be classified into four main categories: left, bilateral, right or absent (Figure S4A) (Long et al., 2003). After scoring, embryos were individually genotyped.

Immunohistochemistry

To visualize the basal body position of each cilium, embryos at 8SS were fixed by MEMFA (3.7% formaldehyde, 0.1M MOPS, 2mM EGTA, 1mM $MgSO_4$) for 2h at room temperature (RT), changed to 100% methanol and stored at $-20°C$ overnight (OV). After rehydration, embryos were washed in PBBT (PBS with 2mg/mL BSA and 0.1% Triton X-100) and blocked in PBBT with 10% goat serum at RT. Subsequently, embryos were incubated OV at $4°C$ with primary antibodies - 1:50 mouse anti-ZO1 antibody and 1:200 mouse anti-gamma tubulin antibody. Afterwards, embryos were washed with PBBT, followed by blocking solution, and incubated OV at $4°C$ with secondary antibody - 1:300 anti-mouse Alexa Fluor 546 IgG. Embryos were finally washed with PBBT and stored in PBS at $4°C$. For imaging, single embryos were flat mounted onto the dish and imaged in a TCS SP8 confocal microscope (*Leica Microsystems*).

Fluid dynamic simulations

We characterized the circulatory flow in the KV by calculating the effective angular velocity vector ($\vec{\Omega}$) as described in (Ferreira et al., 2017). We described each cilium in a KV as a chain of beads moving along a tilted cone with the orientation obtained from 3D-CiliaMap and calculated the flow using Green's function for the Stokes equation in the presence of a spherical no-slip boundary. The effective $\vec{\Omega}$ is defined as the angular velocity of a rotating rigid sphere with the same angular momentum as the time-averaged flow in the KV.

Analysis of cilia basal body positions

To analyze the basal body position of each cilium, embryos at 8SS were fixed by MEMFA and labeled with anti-ZO1 and anti-gamma tubulin antibodies, followed by Alexa Fluor 546 IgG labeling (detailed protocol in "Immunohistochemistry" method section). Afterwards, samples were imaged in a TCS SP8 confocal microscope (*Leica Microsystems*). Cilia basal bodies were segmented in 3D from fluorescence images using Imaris (Bitplane Inc.). A local reference frame at the origin of each basal body was defined to identify the local tangent plane to the vesicle in 3D. Using custom-made scripts in MATLAB (The MathWorks Inc.), the fluorescence intensity of pixels up to $2\mu m$ away from it was orthogonally projected on this plane (Figure S3B) to manually draw the cell contour and extract the antero-posterior (AP) and left-right (LR) extension of the cell. The relative position of the basal body relatively to them has then been calculated for every cilium as shown in Figures S3B and S3C. We note that due to the fixation process, the KV appear flattened in the dorso-ventral direction. As a result, since cell surfaces never appear perfectly orthogonal to the AP or LR axes, it was always possible to define AP and LR displacement of basal bodies. Overall, we analyzed the basal body position in about 75% of all KV cells, without apparent bias in the relative position of cells within the KV, except the fact that cells closer to the equator (equidistant from the dorsal and ventral poles) were the most difficult to analyze. The AP displacement of the basal body was observed in both anterior and posterior sub-population of cells, while slightly stronger in the latter one (Figure S3D).

QUANTIFICATION AND STATISTICAL ANALYSIS

To statistically test the mirror-symmetry in the KV, we used a permutation test (also called randomization test) (Hesterberg et al., 2005). We compute the statistic $|\varphi_{avg\_left} - \varphi_{avg\_right\ mirror}|$, where φ_{avg_left} is the φ angle of the average resultant vector of left cilia and $\varphi_{avg\_right\ mirror}$ is the φ angle of the resultant vector of right cilia after LR mirror symmetry. This statistic is based on the definition of chirality as we test if the left cilia orientation coincides with the mirror image of right cilia. Left and right labels of cilia are then randomly permutated 300,000 times to construct the sampling distribution of possible $|\varphi_{avg\_left} - \varphi_{avg\_right\ mirror}|$ values. The p value is finally estimated as the proportion of permutations resulting in values greater than or equal to the experimental one. We define the structure of the KV as chiral (or asymmetric) when the p value is lower than 0.05 and the null hypothesis ($\varphi_{avg\_left} = \varphi_{avg\_right\ mirror}$) can be rejected. The same test is used to investigate θ mirror-symmetry. The p values of the effective angular velocity vector ($\vec{\Omega}$) of all conditions against the WT were calculated using Welch's test on the dorsal component $\vec{\Omega}_D$.

Each figure states the number of cilia (N_c), as well as the meaning of error bars (95% CI or standard deviation).

DATA AND SOFTWARE AVAILABITILY

Data S1 is a MATLAB file containing all quantified features. This structure array contains eleven fields, corresponding to the following case names:

"wildtype_3ss" for *Tg*(*actb2:*Mmu.*Arl13b-GFP*) embryos at 3SS;
"wildtype_8ss" for *Tg*(*actb2:*Mmu.*Arl13b-GFP*) embryos at 8SS;
"wildtype_9to14ss" for *Tg*(*actb2:*Mmu.*Arl13b-GFP*) embryos at 9-14SS;
"wildtype_6ss" for *Tg*(*actb2:*Mmu.*Arl13b-GFP*) embryos at 6SS;
"dnaaf1_3ss" for *Tg*(*dnaaf1*^{tm317b}*; actb2:*Mmu.*Arl13b-GFP*) embryos at 3SS;
"dnaaf1_8ss" for *Tg*(*dnaaf1*^{tm317b}*; actb2:*Mmu.*Arl13b-GFP*) embryos at 8SS;
"rock2b" for *Tg*(*actb2:*Mmu.*Arl13b-GFP*) embryos at 8SS treated with rock2b morpholino;
"cup" for *Tg*(*cup*^{tc241}*; actb2:Arl13b-GFP*) embryos at 8SS;
"spaw" for *Tg*(*spaw*^{s457}*; actb2:*Mmu.*Arl13b-GFP*) embryos at 8SS;
"bleb" for *Tg*(*actb2:*Mmu.*Arl13b-GFP*) embryos at 8SS treated with the blebbistatin drug;
"trilobite" for *Tg*(*trilobite*^{tc240a}*; actb2:*Mmu.*Arl13b-GFP*) embryos at 8SS.

We indicate cilia base positions and vector components in the body axis basis $(\vec{e}_A, \vec{e}_L, \vec{e}_D)$ or in the local basis $(\vec{e}_f, \vec{e}_n, \vec{e}_m)$, as defined in (Ferreira et al., 2017). Each cilium position on the spheroid surface of the KV is used to quantify cilia orientation angles θ (cilium tilt angle respective to the surface normal) and φ (cilium orientation on the KV cell surface) (Ferreira et al., 2017). In every KVData.[case name], the thirteen following features can be found in sub-fields:

"allRMS" root mean squared error of ellipsoid fitting.
"allMusLocal" cilia orientation vector coordinates in local basis.
"allMusOriented" cilia orientation vector coordinates in body axis basis.
"phiLocal" phi angle in local basis in rad.
"thetaLocal" theta angle in local basis in rad.
"allOriginsOriented" cilia base coordinates projected on the fitted ellipsoid in the body axis basis.
"allCiliaSizes" cilia sizes in μm, -1 if not measured.
"allMotility" cilia motility, 1 if motile, 0 if immotile, -1 if unclear.
"allTypes" cilia type defined as follow, "ok" for a motile cilium with a good estimation of the orientation, "okimmotile" for an immotile cilium with a good estimation of the orientation, "unclearimmotile," for an immotile cilium with an unclear orientation, and "unclear" in the case of both unclear motility and orientation.
"eFlow" ef coordinates in the body axis basis.
"eMer" em coordinates in the body axis basis.
"eNorm" en coordinates in the body axis basis.
"allRadiiEllipsoid" radii of fitted ellipsoid.